RSC Advances

PAPER

View Article Online
View Journal | View Issue

Cite this: *RSC Adv.*, 2017, **7**, 56073

Surface plasmon-driven catalytic reactions on a patterned Co_3O_4/Au inverse catalyst†

Si Woo Lee,[ab] Changhwan Lee,[ab] Kalyan C. Goddeti,[ab] Sun Mi Kim[b] and Jeong Young Park*[ab]

Received 20th September 2017
Accepted 5th December 2017

DOI: 10.1039/c7ra10450b

rsc.li/rsc-advances

We report hot electron- and surface plasmon-driven catalytic reactions on an inverse catalyst that is composed of a reactive cobalt oxide (Co_3O_4) for the catalyst portion and a metal as the source of localized surface plasmon resonance (LSPR). To achieve this scheme, a patterned Co_3O_4/Au nanostructure was fabricated using the nanosphere lithography technique. The enhancement of catalytic activity for CO oxidation on cobalt oxide by the transfer of plasmonic hot carriers generated from the LSPR of Au under light irradiation was observed. We found that the Co_3O_4/Au inverse catalyst exhibited 25–50% higher catalytic activity when under light irradiation. We attribute this enhancement of catalytic activity to the flow of surface plasmon-driven hot carriers that were created by the absorption of photons on the Au metal, followed by injection into the active Co_3O_4 layers.

1 Introduction

Plasmonic metal nanoparticles have been widely used for many applications (*e.g.* catalytic activity, water splitting reactions, biosensors, solar-cell design, and cancer diagnostics).[1–6] Surface plasmon resonance (SPR) is a strong electromagnetic field near the surface of noble metal nanostructures that can occur in plasmonic metal nanostructures by resonant oscillation of free electrons with the same wavelength as the incident photons.[7–9] Recently, many studies have shown the generation of hot electrons with high kinetic energy (1–3 eV) by the electromagnetic decay of surface plasmons at a femtosecond timescale in plasmonic nanostructures under light irradiation and SPR excitation.[10–12] Mukherjee *et al.* revealed that H_2 molecules on Au nanoparticles can dissociate at room temperature because of hot electrons created from surface plasmon decay under visible light irradiation.[13] Lee *et al.* found a steady-state flow of hot electrons generated by localized surface plasmon resonance (LSPR) at a metal–semiconductor junction.[14] Wang *et al.* reported that a high concentration of hot electrons can tunnel through the insulating layer and generate photocurrent in a metal–insulator–metal device.[15]

To fabricate new plasmonic nanostructures with homogeneous size, shape, and interparticle distance of the structures, several nanolithography techniques have been developed (*e.g.* electron beam lithography, focused ion beam lithography, and nanoimprint lithography).[16–18] Furthermore, the nanosphere lithography (NSL) technique is a low-cost fabrication technique that uses 2-dimensional colloidal crystals (*e.g.* 2D arrays of polystyrene and silica nanospheres) as a mask. The advantage of the NSL technique for plasmonic nanostructures is that the LSPR of noble metal nanostructures can be easily controlled in the visible to near-IR region because the aspect ratio that determines the extinction maximum wavelength can be accurately adjusted by varying the size of the nanospheres used as the mask and the thickness of the deposited noble metal.[19]

Conventional catalysts consist of a metal as the catalyst and an oxide or semiconductor as the support for the metal catalyst. It has been demonstrated that the interaction between the metal and the oxide support at their interface (*i.e.* strong metal–support interactions (SMSI)) can affect the catalytic activity with a dependence on the oxidation state of the metal catalyst and the doping state or reducibility of the oxide support.[20–23] In addition, there are some studies that show the influence of hot electrons from the oxide or semiconductor support on the catalytic activity of metal catalysts when under light irradiation.[24–26]

To understand the intrinsic relation between catalytic activity and hot electron flows generated across metal–oxide interfaces, the design of a fresh catalyst model is important.[27] In previous studies, the active site was the metal, which is influenced by hot electrons from an oxide or a semiconductor. The major shortcoming of this conventional catalyst is the short

[a]*Graduate School of EEWS, Korea Advanced Institute of Science and Technology (KAIST), Daejeon, 305-701, Republic of Korea. E-mail: jeongypark@kaist.ac.kr*

[b]*Center for Nanomaterials and Chemical Reactions, Institute for Basic Science, Daejeon, 305-701, Republic of Korea*

† Electronic supplementary information (ESI) available: XRD patterns of the Au nanostructure (Fig. S1). SEM image of triangular Au nanostructure after sonication (Fig. S2). Sample temperature measured by temperature controller with and without light at 523 K (Fig. S3). SEM images (Fig. S4) and XPS spectra (Fig. S5) of the patterned Co_3O_4/Au inverse catalyst before and after CO oxidation. FDTD simulations on the patterned Au nanostructure (Fig. S6). See DOI: 10.1039/c7ra10450b

range of the electron mean free path for the metal, which can de-energize the hot electron before its arrival at the metal surface. Kim *et al.* reported that the change in catalytic activity for CO oxidation on Au/CeO_2 or Pt/GaN catalysts under light irradiation decreased as the size of the Au or Pt nanoparticles increased because of the length of the mean free path of the metal.[24,26] Lee *et al.* found that smaller Pt nanoparticles lead to higher chemicurrent yield (*i.e.* the number of hot electrons detected per molecule of reaction product formed on the Au/TiO_2 nanodiode surface) during hydrogen oxidation, which is associated with the shorter travel length for the hot electrons, compared with their inelastic mean free path.[28] Therefore, the role of the electron mean free path is critical for studying the relationship between catalytic activity and hot electron flow.

Some oxide materials (*e.g.* cobalt oxide (Co_3O_4), cerium oxide (CeO_2) and cuprous oxide (Cu_2O)) are catalytically reactive because these oxide materials can be easily and reversibly oxidized and reduced.[29–31] Among these reactive oxide materials, Co_3O_4 is specifically known as the most catalytically active oxide material for CO oxidation. Haruta and co-workers demonstrated that some base metal oxides (*e.g.* Co_3O_4, MnO_2, and NiO) are intrinsically reactive for CO oxidation without a metal catalyst and that the catalytic activity of base metal oxides decreases in the following order: $Co_3O_4 > MnO > NiO > CuO > Fe_2O_3 > Mn_2O_3 > Fe_3O_4 > CeO_2 > TiO_2$.[32] Xie *et al.* found that Co_3O_4 nanorods with predominantly exposed [110] planes are very reactive and stable for CO oxidation at temperatures as low as −77 °C, giving 100% CO conversion because of the presence of active Co^{3+} species at the surface.[33] Song *et al.* reported that mesoporous cobalt oxide nanoparticle aggregates can achieve 100% CO conversion to CO_2 at −60 °C under normal conditions.[34] It was found that a small Co_3O_4–SiO_2 nanocomposite catalyst prepared using an activated carbon template exhibits very high activity for CO oxidation at −76 °C.[35]

To overcome the short electron mean free path problem in the metal, we used an inverse catalyst in this study that is composed of a reactive oxide for the catalytic portion and a noble metal for the LSPR source. Triangular noble metal nanostructures show much higher surface-enhanced Raman scattering (SERS) activities than flat noble metals because of the large number of confined hot spots between adjacent triangles.[36] Subsequently, we grew Co_3O_4 on a patterned triangular Au nanostructure to make the patterned Co_3O_4/Au inverse catalyst using NSL (Fig. 1a). We studied the catalytic activity for CO oxidation on the patterned Co_3O_4/Au inverse catalyst with and without light irradiation to identify the role of hot electrons from LSPR on the catalytic reaction. The energy band diagram of the Co_3O_4/Au junction (Fig. 1b) shows the transfer of hot electrons and their effect on catalytic activity. The Schottky barrier height for Au/Co_3O_4 is 1.6 eV, which was determined by the difference between the work function of the Au (5 eV) and the electron affinity for Co_3O_4 (3.4 eV).[37] The main merit of our inverse catalyst is the long mean free path in the oxide created by using a reactive oxide material on a plasmonic noble metal. Energetic hot electrons having high kinetic energy (2.0–2.1 eV) formed *via* LSPR upon the absorption of photons on the plasmonic gold. The hot electrons then travelled over the Schottky barrier and arrived at the Co_3O_4 surface because of their long mean free path. Thus, these plasmonic hot carriers can affect the catalytic activity of CO oxidation on Co_3O_4.

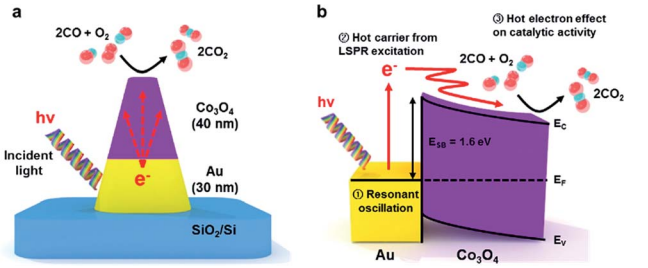

Fig. 1 (a) Schematic drawing of the patterned Co_3O_4–Au nanostructure and the effect of hot electrons on catalytic activity under light irradiation. (b) Energy band diagram for the Au–Co_3O_4 inverse catalyst representing the flow of hot electrons generated from the LSPR of the patterned Au nanostructures and their effect on the CO oxidation reaction when under light irradiation.

2 Experimental

2.1 Fabrication of the two-dimensional patterned Co_3O_4/Au nanostructures by nanosphere lithography

Chemicals. Tetraethyl orthosilicate (TEOS, Aldrich, >99.0%), sodium dodecyl sulfate (SDS, Aldrich, >99.0%), ammonium hydroxide (NH_4OH, Dae Jung Chemicals, 25.0–28.0%), chloroform ($CHCl_3$, Junsei, 99.0%), ethanol (C_2H_5OH, Merck), and methanol (CH_3OH, Merck) were used. 300 nm SiO_2 nanospheres were synthesized using the Stöber method, as follows. 0.55 mL of NH_4OH in 3.5 mL of deionized water was added to 10 mL of ethanol and stirred. 2.3 mL of TEOS in 10 mL of ethanol was injected dropwise into the previous solution. After stirring the reaction solution at room temperature for 12 h, the mixture was centrifuged at 3000 rpm for 10 min and washed with ethanol. After repeating this washing process three times, the 300 nm SiO_2 nanospheres were dispersed in methanol. Self-assembled monolayer arrays of silica nanospheres were prepared on a clean SiO_2/Si substrate by utilizing the Langmuir–Blodgett (LB) technique using a Nima Technology 311D. To spread the SiO_2 nanospheres onto the deionized water subphase in a trough, 3 mg of SDS was mixed with 2 mL of the previous silica solution dispersed in methanol. After ultrasonication of the mixed solution for 40 min with heating, 3 mL of chloroform was added to float the silica nanospheres on the water and sonicated again for 30 min. This prepared solution was spread and floated on the water surface; the surface pressure was monitored using a Wilhelmy plate. While maintaining the target surface pressure at 15 mN m^{-1}, the self-assembled packed silica nanospheres were transferred onto the SiO_2/Si substrate through the monolayer by slowly lifting the substrate at a constant speed of 1 mm min^{-1}. For fabrication of the Co_3O_4/Au nanostructures, thin films consisting of 5 nm of titanium (Ti), 30 nm of gold (Au), and 40 nm of cobalt (Co) were deposited sequentially using electron beam evaporation on the previously closely packed SiO_2 nanospheres on SiO_2/Si

substrate. At room temperature, all the thin films were deposited using 10 kV DC voltage in a high-vacuum chamber with a base pressure of 5×10^{-7} Torr, evacuated using rotary pumps and turbo molecular pumps. The metal deposition rate was 0.1 Å s^{-1} until 2 nm was deposited for adhesion. The deposition rate was then increased to 0.5 Å s^{-1} until reaching the final metal thickness. The closely packed SiO_2 nanosphere arrays act as a mask, thus all the metal was deposited with the SiO_2 nanospheres creating the patterning. After finishing the metal deposition, the cobalt was oxidized to Co_3O_4 by heat treatment at 553 K for 2 h 30 min. Finally, the 300 nm SiO_2 nanospheres were removed by sonication for 1 minute with deionized water. The patterned Co_3O_4–Au islands were thus obtained using NSL. Based on our experience fabricating Au/TiO_2 catalytic nanodiodes, in the case of the Au/Ti interface, the electrical contact is an ohmic contact and is very unlikely to have a Schottky barrier. To form a Schottky barrier, we would need to heat the Ti layer under oxygen to form TiO_2 before depositing the Au layer.

2.2 Characterization, chemical modification, and structures of the patterned Co_3O_4/Au nanostructures

The crystalline phases of the cobalt oxide and the Au nanostructure before and after heat treatment were revealed using X-ray diffraction patterns (XRD, Rigaku D/MAX-2500) taken at a 2θ scan range of 10–70°, scan speed of 4° min^{-1}, and step size of 0.01 Å using Cu Kα radiation. The oxidation state of the cobalt oxide (Co 2p) before and after CO oxidation was identified using X-ray photoelectron spectroscopy (XPS, Thermo VG Scientific Sigma Probe system with an Al Kα X-ray source (1486.3 eV)) with an energy resolution of 0.47 eV full width at half maximum (FWHM) under ultrahigh vacuum (10^{-10} Torr). The thickness and morphology of the patterned Co_3O_4/Au nanostructures were characterized using cross-section transmission electron microscopy (TEM, FEI Titan G2 Cubed 60-300), scanning transmission electron microscopy and high-angle annular dark field (STEM-HAADF, FEI Titan G2 Cubed 60-300), corresponding energy-dispersive X-ray spectroscopy (EDS, FEI Super X (4 SDD EDS)) elemental maps for 300 s, energy-dispersive X-ray spectroscopy (EDS) line profiles, and scanning electron microscopy (SEM, Magellan 400). The TEM specimen was prepared using the focused ion beam (FIB, Helios Nanolab 450 F1) preparation technique for cutting cross sections of the Co_3O_4/Au nanostructures. Two sizes of triangular Au nanostructures were created by changing the size of the SiO_2 nanosphere mask. The optical properties of these Au nanostructures were characterized using a UV-vis spectrophotometer (Lambda 1050). Triangular Au nanostructures (30 nm high) were prepared on a quartz window (1 mm thick) using the same method described previously. The spectral range was 400–800 nm, and a clean quartz window was used as a reference.

2.3 Measurement of the catalytic activity of CO oxidation on patterned Co_3O_4/Au inverse catalysts with and without light irradiation

Reaction studies were performed in an ultrahigh vacuum chamber (1 L) with a base pressure of 1×10^{-8} Torr, evacuated using rotary pumps and turbo molecular pumps. After isolating with a gate valve, the CO oxidation reaction was carried out in the batch reactor system under 40 Torr CO and 100 Torr O_2 as the reactant gases and 620 Torr He as the balancing gas. All the gases were circulated continuously through the reaction line by a Metal Bellows recirculation pump at a rate of 2 L min^{-1}. After 30 min of recirculation at room temperature for gas equilibration, a DS 6200 gas chromatograph (GC) equipped with a thermal conductivity detector and a 6 in. × 1/8 in. SS molecular sieve 5A was used to separate the products for analysis. The CO conversion was monitored at various temperatures (523–553 K) and the measured reaction rates were reported as turnover frequencies (TOF), which were measured in units of product molecules of CO_2 produced per active Co_3O_4 surface site per second of reaction time. All the reaction data were obtained by measuring the rate of CO oxidation at low conversion (*i.e.*, conversion below ~15%) to check the initial reaction rate within a kinetically controlled regime, assuming different reaction conditions. The number of active sites was calculated from the geometry in the SEM measurements of the surface area of the nanoparticle arrays. A halogen lamp (Dolhan-Janner D150) was used as the light source to measure the enhancement of catalytic activity while under light irradiation. The distance between the sample and halogen lamp was about 8 cm through a sapphire window and the light intensity was measured to be 49.4 mW cm^{-2} at this distance by an optical power meter (ADCMT 8230).

2.4 Finite-difference time domain (FDTD) simulations

The distributions of the electric field by localized surface plasmon resonance (LSPR) on the patterned Co_3O_4–Au nanostructure and the patterned Au nanostructure were calculated using a two-dimensional FDTD simulation with a commercial FDTD simulation package (FDTD-Lumerical™). The optical properties of the gold were obtained from the materials database in the software using the Drude model. The refractive index of Co_3O_4 was obtained experimentally using a spectroscopic ellipsometer (Woollam M2000D). Variable angle spectroscopic ellipsometric (VASE) data (*i.e.* 65.00, 70.00, 75.00°) were acquired from a Co_3O_4 thin film on a SiO_2 wafer (173 nm cobalt oxide/1000 nm SiO_2) and modelled in B-spline mode to calculate the refractive index for cobalt oxide (2.8 at 622 nm). The electric field distribution was acquired with a mesh size of 0.5 nm at an incident light of 622 nm, which is the extinction maximum wavelength (λ_{ex}) of the nanostructures derived from the UV-vis absorbance spectra. The geometric model used in these calculations for the patterned Co_3O_4/Au nanostructure and the patterned Au nanostructure was built from the SEM and TEM images.

3 Results and discussion

3.1 Characterization of the patterned Co_3O_4/Au inverse catalysts

We fabricated reactive oxide/plasmonic noble metal hybrid structures using the NSL technique. The Co_3O_4 on triangular Au

nanostructures were thus fabricated: first, 300 nm SiO_2 nanospheres were synthesized using the well-known Stöber method, and self-assembled monolayer arrays of silica nanospheres were prepared on a clean SiO_2/Si substrate using the LB technique. Next, 30 nm of gold as the LSPR source and 40 nm of cobalt as the catalyst were deposited sequentially by electron beam evaporation on the previously fabricated closely packed SiO_2 nanospheres on SiO_2/Si substrate. The closely packed SiO_2 nanosphere arrays act as a mask so that all the metal was deposited using the SiO_2 nanospheres for patterning. Finally, the cobalt was oxidized to Co_3O_4 by heat treatment at 553 K for 2 h 30 min and the 300 nm SiO_2 nanospheres were removed by sonication for 1 minute with deionized water, thus obtaining the patterned Co_3O_4–Au islands. All the fabrication procedures and SEM images are shown in Fig. 2a–d and e–h, respectively.

Fig. 3a shows the crystalline phase of the cobalt oxide according to annealing temperature, as revealed by XRD patterns. After annealing at 553 K, diffraction peaks corresponding to a cubic spinel structure were confirmed, indicating that the cobalt was fully oxidized to Co_3O_4. Co_3O_4 has a cubic spinel structure and the Au nanostructure was polycrystalline after annealing at 553 K, as shown in Fig. 3a and S1 in ESI.† Fig. 3b illustrates the UV-vis extinction spectra of the 30 nm triangular Au nanostructures fabricated by NSL using 200 and 300 nm SiO_2 nanospheres as masks. All the Au cones remained and there were no SiO_2 nanospheres after sonication, as shown in Fig. S2 in ESI.† It is well known that the optical properties (*e.g.* the intensity and extinction maximum wavelength) of the LSPR for noble metal nanoparticles are influenced by shape, size, and dielectric environment. Previous studies show that the extinction maximum wavelength of triangular noble metal nanostructures fabricated by NSL can be tuned by changing the aspect ratio (*i.e.* the ratio of the length and the height) of the triangular nanostructures.[38,39] In this work, the aspect ratio was controlled by changing the size of the SiO_2 nanospheres used as the mask. The extinction maximum wavelength peak of the triangular Au nanostructures from the 300 nm SiO_2 nanospheres was red-shifted from the wavelength peak of the triangular Au nanostructures from the 200 nm SiO_2 nanospheres because of the increased aspect ratio from the large SiO_2 nanospheres, which reveals that the extinction spectrum represents absorption by the LSPR of the triangular Au

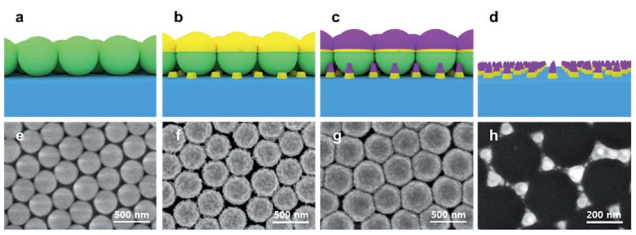

Fig. 2 Fabrication procedure for the patterned Co_3O_4–Au nanostructures and corresponding SEM images. (a and e) Deposition of 300 nm SiO_2 nanospheres using the LB technique. (b and f) E-Beam deposition of 30 nm of Au. (c and g) E-Beam deposition of 40 nm of Co. (d and h) Heat treatment for oxidation of the cobalt to cobalt oxide and removal of the SiO_2 nanospheres.

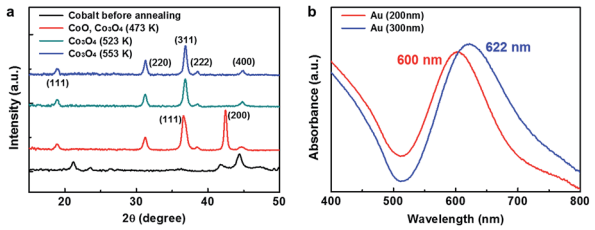

Fig. 3 (a) XRD patterns of the cobalt oxide at different annealing temperatures. (b) UV-visible absorbance spectra of the patterned Au nanostructures fabricated using 200 or 300 nm SiO_2 spheres.

nanostructures. In addition, there was an ultraweak absorption band about 750 nm away from the extinction maximum wavelength peak. This broad LSPR band came from some defects in the triangular Au nanostructures that were caused by misalignment of the SiO_2 nanospheres or by the size distribution of the SiO_2 nanospheres, as shown in Fig. S2 in ESI.†[39]

To identify the thickness and morphology of the patterned Co_3O_4/Au nanostructures, a cross-sectional TEM image was taken (Fig. 4a). During fabrication of the Co_3O_4/Au nanostructures, vacancies between three closely packed SiO_2 nanosphere arrays created cobalt oxide/Au nanostructures with nanopyramidic shape. Fig. 4d–h shows a STEM-HAADF image and EDS elemental maps for 300 s of the patterned Co_3O_4/Au nanostructure. It clearly shows that the top layer is cobalt oxide (*i.e.* the catalyst portion) and that there is a Au triangle under the cobalt oxide (*i.e.* the LSPR source). An EDS line profile of the patterned Co_3O_4/Au nanostructure is shown in Fig. 4b and c. The heights of the Au triangle and cobalt oxide are 30 and 40 nm, respectively.

3.2 Surface-plasmon driven CO oxidation on patterned Co_3O_4/Au inverse catalysts

Here, we carried out CO oxidation on the patterned Co_3O_4/Au inverse catalyst with and without light to show the intrinsic relation between catalytic activity and hot electron flow from the LSPR on the triangular Au nanostructure during light irradiation. Reaction studies were performed in an ultrahigh vacuum chamber (1 L) with a base pressure of 1×10^{-8} Torr, evacuated

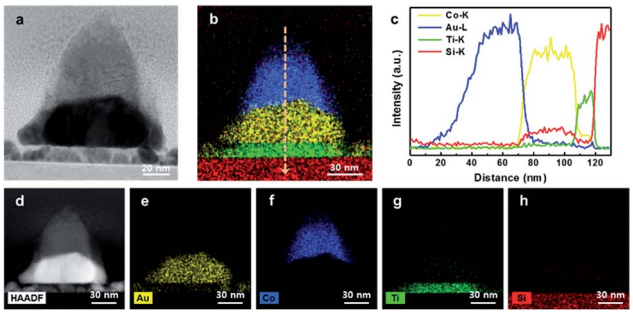

Fig. 4 (a) TEM image of the Co_3O_4–Au nanostructure. (b and c) EDS line profile of the Co_3O_4–Au nanostructure. (d) STEM-HADDF image of the Co_3O_4–Au nanostructure and (e–h) EDS elemental maps of each component.

using rotary and turbo molecular pumps. After isolation using a gate valve, the CO oxidation reaction was carried out in the batch reactor system under 40 Torr CO and 100 Torr O_2 as the reactant gases and 620 Torr He as the balancing gas. CO conversion was monitored at various temperatures (523–553 K) and the measured reaction rates were reported as TOF, which are measured in units of product molecules of CO_2 produced per active Co_3O_4 surface site per second of reaction time.

Fig. 5a and b shows the catalytic activity for CO oxidation measured on the patterned Co_3O_4/Au inverse catalyst at four different temperatures (523–553 K) with and without light. The patterned Co_3O_4/Au inverse catalyst shows a higher catalytic activity under light irradiation than in the dark. Previous studies show that the enhancement of the activity of the Pt NPs/p-doped GaN wafer under light irradiation was 11–33% which was measured using the same batch reactor system and halogen lamp as used in this study;[26] thus, the enhancement under light irradiation (25–50%) observed on the Co_3O_4/Au inverse catalyst is significant. It is associated with hot electrons generated from LSPR excitation of the triangular Au nanostructure by light absorption that can affect the catalytic activity for CO oxidation on the reactive Co_3O_4. However, the thermal effect of light irradiation can also result in the enhancement of catalytic activity. We measured sample temperature data with a temperature controller with and without light at 523 K under 40 Torr CO, 100 Torr O_2, and 620 Torr He (Fig. S3 in ESI†). There was no change in the sample temperature when light was irradiated on the sample, demonstrating that any heating effect by light irradiation can be ignored in our experiments. Also some previous studies show a decrease in catalytic activity for CO oxidation on Pt/n-Si and Pt nanoparticle/n-type GaN resulting from a reduced net charge on the Pt nanoparticles when under light irradiation.[25,26,40] CO oxidation was also carried out on the patterned Co_3O_4 nanostructure with and without light under the same conditions to compare the catalytic activity of the patterned Co_3O_4/Au inverse catalyst (Fig. 5c). Under light irradiation, the catalytic activity of the Co_3O_4 exhibited an insignificant difference (*i.e.* within the error of measurement). Even if a hot electron is generated on the Co_3O_4 from electron–hole pair excitation when under light irradiation, it will eventually turn into a low-energy electron through inelastic scattering within a time scale of femtoseconds. Hot electrons from LSPR excitation on Au can be transferred when a metal–oxide interface is formed, revealing that a role for Au nanostructures is as an LSPR excitation source, leading to a change in catalytic activity for CO oxidation. The TOF values of the patterned Co_3O_4/Au inverse catalyst were similar to the TOF values of the patterned Co_3O_4 nanostructure in the same reaction temperature range, demonstrating that there was no synergetic effect between the Au and the Co_3O_4. We also carried out CO oxidation on the patterned Au nanostructure at 573 K without Co_3O_4, but there was no CO_2 product although the triangular Au nanostructure was polycrystalline. Thus, the CO oxidation reaction was occurring on the Co_3O_4, and not on the Au nanostructure. While the triangular Au nanostructure is not reactive in this reaction temperature range, it does perform a role as the LSPR source when under light irradiation. Hence, we can confirm that the enhancement of catalytic activity only originated from hot carriers generated by LSPR excitation of the Au that were then transferred to the reactive Co_3O_4.

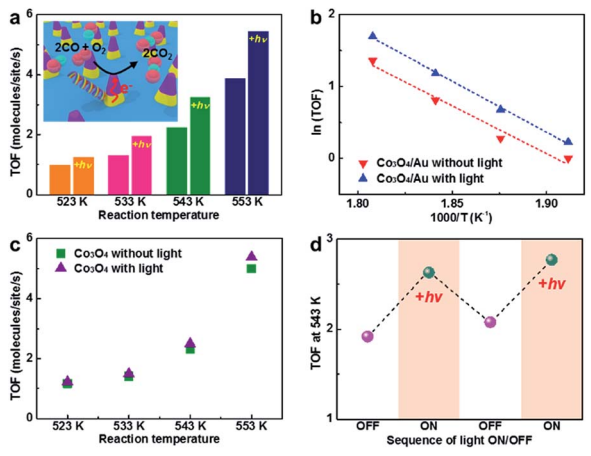

Fig. 5 (a) Catalytic activity for CO oxidation on the patterned Co_3O_4–Au inverse catalyst with and without light at four different temperatures. (b) Arrhenius plots of the patterned Co_3O_4–Au inverse catalyst with and without light at four different temperatures. (c) Catalytic activity for CO oxidation on the patterned Co_3O_4 nanostructure with and without light at four different temperatures. (d) TOF for CO oxidation with sequential light ON/OFF on the patterned Co_3O_4/Au at 543 K. The TOF value was calculated from the slope of the turnover number with time.

To confirm whether the plasmonic hot carrier effect on catalytic activity was reversible, CO oxidation was carried out continuously on the patterned Co_3O_4/Au inverse catalyst as the light was turned on and off at 543 K (Fig. 5d). The TOF value was similar to prior experiments (Fig. 5a): the catalytic activity was enhanced and then returned to the original catalytic activity as the halogen lamp was turned on and off, respectively, showing that the plasmonic hot carrier effect from the triangular Au nanostructure to the Co_3O_4 was reversible. The small increase in the TOF value in the second cycle was the result of calcination of the sample during the reaction. After the reaction, the morphology of the patterned Co_3O_4/Au nanostructure had minor changes, but there were no significant morphology changes, as verified by SEM images taken before and after the CO oxidation reaction (Fig. S4 in ESI†). XPS measurements showed that the oxidation state of the cobalt oxide was a mixture of Co^{2+} and Co^{3+}, representing Co_3O_4. After the reaction, a higher percentage of Co^{3+} was observed (Fig. S5 in ESI†).

To understand the electric field distribution from the LSPR around the patterned Co_3O_4–Au nanostructure, we carried out two-dimensional FDTD simulation analysis. The electric field distribution was obtained with a mesh size of 0.5 nm and incident light of 622 nm, which corresponds to the extinction maximum wavelength of the nanostructures from the UV-vis absorbance spectra. We set the refractive index of the Co_3O_4 at 622 nm to 2.8, which was acquired experimentally, and the geometric model for the patterned Co_3O_4/Au nanostructure was built on experimentally observed structural parameters from SEM and TEM images. The calculated simulation results show

an electric field distribution that indicates an enhancement of light absorption for the top and cross-section views of the nanostructure. Fig. 6a shows that the electric field was formed around the vertex points of the patterned Au nanostructure, which was oriented along the direction of polarization. In Fig. 6b, the electric field was confined prominently along the gold edge between two adjacent Au triangles. In particular, a strong electric field was formed at the interface between the Au and Co_3O_4 due to the higher refractive index of the Co_3O_4.[41] For the patterned Au nanostructure without Co_3O_4, there was no electric field on the top surface of the Au nanostructure and the electric field was formed only along the side of the Au nanostructure (Fig. S6 in ESI†). This interesting LSPR confined at the Au–Co_3O_4 interface can support the plausible hot electron transfer mechanism, indicating that the generated hot electrons at the Au edge or the Au–Co_3O_4 interface were transferred to the Co_3O_4 over the Schottky barrier and can easily transfer to the Co_3O_4 surface owing to their long electron mean free path affecting the catalytic activity on the cobalt oxide.

CO molecules are known to be well adsorbed on Co_3O_4, especially on the Co^{3+} site, and the mechanism for CO oxidation over Co_3O_4 is believed to the Mars–van Krevelen type in which CO molecules adsorb on the Co_3O_4 surface and react with lattice oxygen at Co_3O_4 followed by O_2 filling in the oxygen vacancy of the Co_3O_4.[32,42] We can explain that the enhancement of catalytic activity when under light irradiation is attributed to the Co_3O_4 surface becoming negatively charged by hot electrons from LSPR excitation of the triangular Au nanostructure. Previous studies used ambient-pressure X-ray photoelectron spectroscopy (APXPS) and near edge X-ray adsorption fine structure spectroscopy (NEXAFS) to show that the main reaction intermediate for CO oxidation on Cu-based catalysts is adsorbed $CO_2^{\delta-}$.[43] Maximoff *et al.* shows that partially charged oxygen ($O^{\delta-}$) can react with CO and produce $CO_2^{\delta-}$ (*i.e.* the partially negatively charged reaction intermediate), and finally produce CO_2 and generate chemicurrent.[44] Calaza *et al.* reported that electrons are shuttled from the ultrathin MgO(001) film grown on Ag(001) to Au islands, thus inducing the formation of a negative CO_2 radical that reacts to form an oxalate.[45] There are also earlier studies showing that the catalytic activity of CO oxidation on Pt catalysts supported on F-doped TiO_2 was enhanced by O activation because of electron spillover from the highly n-type TiO_2.[22] The mechanism for electron spillover is still not clear; it was postulated that electrons in the highly doped TiO_2 can activate lattice oxygen in the TiO_2, which is then followed by CO oxidation with adsorbed CO at the Pt/TiO_2 interface in a Mars–van Krevelen type mechanism.[46] In our studies, hot electrons at negatively charged Co_3O_4 can transfer to the lattice oxygen at Co_3O_4 and produce CO_2 through the reaction intermediate ($CO_2^{\delta-}$), O (Co_3O_4) + δe^- → $O^{\delta-}$ (Co_3O_4), CO(g) + $O^{\delta-}$ (Co_3O_4) → $CO_2^{\delta-}$(ad) → CO_2(g); or transfer to the reaction intermediate ($CO_2^{\delta-}$) and produce gas-phase CO_2, CO(g) + O (Co_3O_4) → CO_2(ad), CO_2(ad) + δe^- → $CO_2^{\delta-}$(ad) → CO_2(g). Thus, hot electrons from LSPR excitation of the triangular Au nanostructure can easily transfer to the Co_3O_4 surface because of their long electron mean free path, and the negatively charged species can transfer to lattice oxygen at Co_3O_4 or adsorbed CO_2 to generate negatively charged oxygen ($O^{\delta-}$) or adsorbed CO_2 ($CO_2^{\delta-}$), which play important roles for CO_2 production from CO and oxygen *via* the Mars–van Krevelen type mechanism.

Another possible mechanism for explaining the enhancement of catalytic activity by LSPR of the triangular Au nanostructure under light irradiation is the partial reduction of Co^{3+} to Co^{2+}. Marimuthu *et al.* reported that selectivity for propylene oxide in propylene epoxidation increases on the Cu_2O shell–metallic Cu core structure when under light irradiation. They found that Cu_2O was reduced to metallic Cu, which is attributed to LSPR of the metallic copper under visible light irradiation using an *in situ* UV-vis extinction experiment.[47] Kim *et al.* demonstrated the reduction of Fe^{3+} ions bound to a cyanide/Ag nanoparticle system induced by plasmonically generated hot electrons from the Ag nanoparticles.[48] Also, Li *et al.* reported the selectivity of benzyl alcohol oxidation to benzaldehyde on a gold core@ceria shell catalyst under visible light irradiation that resulted from reducing Ce^{4+} to Ce^{3+} by hot electron transfer from the LSPR of the gold core to the CeO_2 shell.[30] Shen and coworkers found that Co_3O_4 nanorods with predominantly exposed [110] planes are very catalytically active for CO oxidation at low temperature, giving 100% CO conversion because of the presence of active Co^{3+} species at the surface. This unexpected catalytic reactivity of Co_3O_4 nanorods for CO oxidation is explained in the following mechanism: Co_3O_4 has a spinel structure containing Co^{3+} in an octahedral coordination and Co^{2+} in a tetrahedral coordination. In these surface atomic configurations, there are only Co^{2+} cations on the [001] and [111] planes, which are almost inactive, while the [110] plane is mainly composed of Co^{3+} cations, which are regarded as the active site for CO oxidation. Thus, CO only adsorbs on the surface Co^{3+} site and oxidation of the adsorbed CO then occurs by abstracting the surface oxygen that was coordinated with the Co^{3+} cations. The Co^{3+} cations are partially reduced to Co^{2+} and, finally, the partially reduced cobalt oxide can be re-oxidized by a gas-phase oxygen molecule to become active Co^{3+} cations again.[33] The reaction between the adsorbed CO on Co^{3+} and the lattice oxygen is the overall rate-determining step in CO oxidation.[42] Broqvist *et al.* performed a first-principles density functional theory (DFT) study regarding the CO oxidation mechanism at the Co_3O_4(110) surface and found that the reduction of Co^{3+} to Co^{2+} (Co^{3+} + e^- → Co^{2+}) in Co_3O_4(110) is crucial for the O abstraction step for CO_2 formation.[49] Here, in our patterned Co_3O_4–Au inverse catalysts, if a negatively

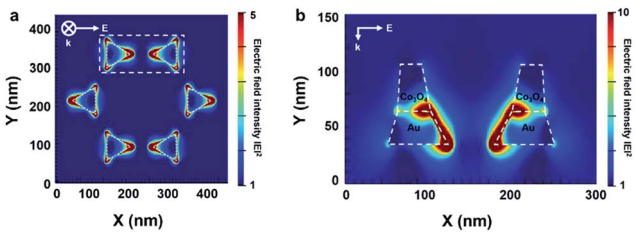

Fig. 6 FDTD calculations of the electric field intensity from LSPR on the patterned Co_3O_4–Au nanostructure: (a) top view and (b) cross-section view.

charged hot electron from LSPR excitation on Au is transferred to the cobalt oxide, reduction of the cobalt oxide can occur, which is a decisive step for CO oxidation.

To find the exact mechanism for the enhancement of catalytic activity at the cobalt oxide by hot electron transfer from the Au, theoretical DFT studies or *in situ* spectroscopic and microscopic experiments (*e.g.* ambient-pressure techniques) are needed for these catalysts under light irradiation. But our studies here on these reactive oxide/plasmonic noble metal inverse catalysts can connect the enhancement of catalytic activity to LSPR excitation from the metal, having possible applications for surface plasmon-based oxide/metal hybrid nanocatalysts or catalytic nanodiodes because of the long electron mean free path of the oxide materials.

4 Conclusions

In summary, Co_3O_4 is known as a reactive oxide material for CO oxidation. Triangular noble metal nanostructures fabricated using the NSL technique exhibit higher SERS activities than flat noble metals. We used cobalt oxide as the catalytic portion and a triangular Au nanostructure as the SPR source for the patterned Co_3O_4/Au nanostructure. The patterned Co_3O_4/Au inverse catalyst nanostructures were prepared using the NSL technique with SiO_2 nanospheres as the mask for metal deposition by electron beam evaporation. FDTD simulations showed that a particularly strong electric field was formed at the Au–Co_3O_4 interface because of the higher refractive index of the Co_3O_4. CO oxidation on the patterned Co_3O_4/Au nanostructure was carried out with and without light to find the relationship between hot electron transfer to the reactive oxide from LSPR excitation on the triangular Au nanostructure and the change in catalytic activity for CO oxidation. The patterned Co_3O_4–Au inverse catalysts showed 25–50% higher catalytic activity for CO oxidation when under light irradiation than in the dark. The reversibility of the plasmonic hot carrier effect on catalytic activity was confirmed by observation of two catalytic activities with the light turned on and off, respectively. The change in catalytic activity implies that hot carriers generated from LSPR excitation of the Au nanostructure by absorption of photons on the Au metal can transfer to the Co_3O_4, and thus reversibly enhance the catalytic activity for CO oxidation.

Conflicts of interest

There are no conflicts to declare.

Acknowledgements

This work was supported by the Institute for Basic Science (IBS) [IBS-R004-A2-2017-a00].

Notes and references

1 S. Linic, U. Aslam, C. Boerigter and M. Morabito, *Nat. Mater.*, 2015, **14**, 567.
2 H. A. Atwater and A. Polman, *Nat. Mater.*, 2010, **9**, 205.
3 W. H. Hung, M. Aykol, D. Valley, W. Hou and S. B. Cronin, *Nano Lett.*, 2010, **10**, 1314–1318.
4 D. B. Ingram and S. Linic, *J. Am. Chem. Soc.*, 2011, **133**, 5202–5205.
5 J. N. Anker, W. P. Hall, O. Lyandres, N. C. Shah, J. Zhao and R. P. Van Duyne, *Nat. Mater.*, 2008, **7**, 442–453.
6 I. H. El-Sayed, X. Huang and M. A. El-Sayed, *Nano Lett.*, 2005, **5**, 829–834.
7 W. L. Barnes, A. Dereux and T. W. Ebbesen, *Nature*, 2003, **424**, 824.
8 K. A. Willets and R. P. Van Duyne, *Annu. Rev. Phys. Chem.*, 2007, **58**, 267–297.
9 S. Eustis and M. A. El-Sayed, *Chem. Soc. Rev.*, 2006, **35**, 209–217.
10 C. Clavero, *Nat. Photonics*, 2014, **8**, 95–103.
11 J. Endriz and W. Spicer, *Phys. Rev. Lett.*, 1970, **24**, 64.
12 M. W. Knight, H. Sobhani, P. Nordlander and N. J. Halas, *Science*, 2011, **332**, 702–704.
13 S. Mukherjee, F. Libisch, N. Large, O. Neumann, L. V. Brown, J. Cheng, J. B. Lassiter, E. A. Carter, P. Nordlander and N. J. Halas, *Nano Lett.*, 2013, **13**, 240–247.
14 Y. K. Lee, C. H. Jung, J. Park, H. Seo, G. A. Somorjai and J. Y. Park, *Nano Lett.*, 2011, **11**, 4251–4255.
15 F. Wang and N. A. Melosh, *Nat. Commun.*, 2013, **4**, 1711.
16 E. M. Hicks, S. Zou, G. C. Schatz, K. G. Spears, R. P. Van Duyne, L. Gunnarsson, T. Rindzevicius, B. Kasemo and M. Käll, *Nano Lett.*, 2005, **5**, 1065–1070.
17 E. Vesseur, R. De Waele, H. Lezec, H. Atwater, F. García de Abajo and A. Polman, *Appl. Phys. Lett.*, 2008, **92**, 083110.
18 K. Li, L. Clime, B. Cui and T. Veres, *Nanotechnology*, 2008, **19**, 145305.
19 H. Ko, S. Singamaneni and V. V. Tsukruk, *Small*, 2008, **4**, 1576–1599.
20 K. An, S. Alayoglu, N. Musselwhite, S. Plamthottam, G. r. m. Melaet, A. E. Lindeman and G. A. Somorjai, *J. Am. Chem. Soc.*, 2013, **135**, 16689–16696.
21 L. R. Baker, G. Kennedy, M. Van Spronsen, A. Hervier, X. Cai, S. Chen, L.-W. Wang and G. A. Somorjai, *J. Am. Chem. Soc.*, 2012, **134**, 14208–14216.
22 L. R. Baker, A. Hervier, H. Seo, G. Kennedy, K. Komvopoulos and G. A. Somorjai, *J. Phys. Chem. C*, 2011, **115**, 16006–16011.
23 S. Tauster, S. Fung, R. Baker and J. Horsley, *Science*, 1981, **211**, 1121–1125.
24 S. M. Kim, H. Lee, K. C. Goddeti, S. H. Kim and J. Y. Park, *J. Phys. Chem. C*, 2015, **119**, 16020–16025.
25 S. M. Kim, S. J. Lee, S. H. Kim, S. Kwon, K. J. Yee, H. Song, G. A. Somorjai and J. Y. Park, *Nano Lett.*, 2013, **13**, 1352–1358.
26 S. M. Kim, D. Park, Y. Yuk, S. H. Kim and J. Y. Park, *Faraday Discuss.*, 2013, **162**, 355–364.
27 J. Y. Park, S. M. Kim, H. Lee and I. I. Nedrygailov, *Acc. Chem. Res.*, 2015, **48**, 2475–2483.
28 H. Lee, I. I. Nedrygailov, C. Lee, G. A. Somorjai and J. Y. Park, *Angew. Chem., Int. Ed.*, 2015, **54**, 2340–2344.
29 F. Yang, J. Graciani, J. Evans, P. Liu, J. Hrbek, J. F. Sanz and J. A. Rodriguez, *J. Am. Chem. Soc.*, 2011, **133**, 3444–3451.

30 B. Li, T. Gu, T. Ming, J. Wang, P. Wang, J. Wang and J. C. Yu, *ACS Nano*, 2014, **8**, 8152–8162.
31 G. Jernigan and G. Somorjai, *J. Catal.*, 1994, **147**, 567–577.
32 Y. Yu, T. Takei, H. Ohashi, H. He, X. Zhang and M. Haruta, *J. Catal.*, 2009, **267**, 121–128.
33 X. Xie, Y. Li, Z.-Q. Liu, M. Haruta and W. Shen, *Nature*, 2009, **458**, 746.
34 W. Song, A. S. Poyraz, Y. Meng, Z. Ren, S.-Y. Chen and S. L. Suib, *Chem. Mater.*, 2014, **26**, 4629–4639.
35 C.-J. Jia, M. Schwickardi, C. Weidenthaler, W. Schmidt, S. Korhonen, B. M. Weckhuysen and F. Schüth, *J. Am. Chem. Soc.*, 2011, **133**, 11279–11288.
36 M. Tabatabaei, A. Sangar, N. Kazemi-Zanjani, P. Torchio, A. Merlen and F. o. Lagugné-Labarthet, *J. Phys. Chem. C*, 2013, **117**, 14778–14786.
37 S. Chen and L.-W. Wang, *Chem. Mater.*, 2012, **24**, 3659–3666.
38 W. Huang, W. Qian and M. A. El-Sayed, *J. Phys. Chem. B*, 2005, **109**, 18881–18888.
39 S. K. Cushing, J. Li, J. Bright, B. T. Yost, P. Zheng, A. D. Bristow and N. Wu, *J. Phys. Chem. C*, 2015, **119**, 16239–16244.
40 L. R. Baker, A. Hervier, G. Kennedy and G. A. Somorjai, *Nano Lett.*, 2012, **12**, 2554–2558.
41 Z. W. Seh, S. Liu, M. Low, S. Y. Zhang, Z. Liu, A. Mlayah and M. Y. Han, *Adv. Mater.*, 2012, **24**, 2310–2314.
42 H.-F. Wang, R. Kavanagh, Y.-L. Guo, Y. Guo, G. Lu and P. Hu, *J. Catal.*, 2012, **296**, 110–119.
43 B. Eren, C. Heine, H. Bluhm, G. A. Somorjai and M. Salmeron, *J. Am. Chem. Soc.*, 2015, **137**, 11186–11190.
44 S. N. Maximoff and M. P. Head-Gordon, *Proc. Natl. Acad. Sci. U. S. A.*, 2009, **106**, 11460–11465.
45 F. Calaza, C. Stiehler, Y. Fujimori, M. Sterrer, S. Beeg, M. Ruiz-Oses, N. Nilius, M. Heyde, T. Parviainen and K. Honkala, *Angew. Chem., Int. Ed.*, 2015, **54**, 12484–12487.
46 J. Y. Park, L. R. Baker and G. A. Somorjai, *Chem. Rev.*, 2015, **115**, 2781–2817.
47 A. Marimuthu, J. Zhang and S. Linic, *Science*, 2013, **339**, 1590–1593.
48 K. Kim, S. H. Lee, J.-Y. Choi and K. S. Shin, *J. Phys. Chem. C*, 2014, **118**, 3359–3365.
49 P. Broqvist, I. Panas and H. Persson, *J. Catal.*, 2002, **210**, 198–206.